Indian Journal of Pure & Applied Physics
Vol. 64, October 2026, pp. 1092-1106
DOI: 10.56042/ijpap.v64i10.27824

Simulation Analysis of Mixed Contact using Finite Element Method Stress Behavior of Elastoplastic Material

Mohammed Bentahar[a], Noureddine Mahmoudi[a*] & Youcef Moulai Arbi[b]

[a]Department of Civil Engineering and Hydraulics, University of Saida Dr Moulay Tahar, Saida 20000, Algeria

[b]Laboratory of Quantum Physics of Matter and Mathematical Modeling, Mustapha Stambouli University, Mascara 29000, Algeria

Received: 23rd January 2026; accepted: 27th July 2026

This paper presents a numerical investigation of mixed elastoplastic contact between a cylindrical wire and a flat rectangular plate using the Adaptive Mixed Contact Finite Element Method (AMC-FEM). The influence of contact geometry and frictional conditions on contact behavior is analyzed for both single- and double-contact configurations. The effects of wire diameter (5, 10, and 15 mm), contact spacing (20, 25, and 33 mm), and coefficients of friction (0.3, 0.5, and 1.0) are examined under a constant normal load. The numerical results are evaluated in terms of real contact area, normal contact force, stress distribution, and artificial strain energy. The results show that increasing wire diameter enlarges the contact area and redistributes contact pressure, leading to reduced local stress concentrations despite higher normal forces. Friction significantly affects stress asymmetry, stick–slip behavior, and energy dissipation. In double-contact configurations, increasing the distance between contact zones reduces peak stresses and limits interaction effects. The numerical results exhibit qualitative behavior consistent with Hertzian contact theory in the elastic regime while capturing elastoplastic and frictional effects beyond classical models. The proposed approach provides a reliable numerical framework for the analysis and design of mixed contact interfaces in engineering applications.

Keywords: Contact, AMC-FEM, Elastoplastic material, Coefficient of friction (COF), Round wire, Rectangular plate, 2D

1 Introduction

Contact problems are recognized as a fundamental topic in solid mechanics, since contact constitutes the primary mechanism through which external loads are transmitted to deformable bodies. The resulting stress concentrations often represent the most critical regions within a structure and govern its mechanical integrity and durability. A comprehensive overview of the theoretical foundations and analytical solutions in contact mechanics has been presented in the literature[1], highlighting the significance of surface interactions, stress distributions, and deformation mechanisms at contact interfaces.

The finite element method (FEM) has been widely employed to investigate contact-related phenomena. Numerical simulations have been used to analyze the evolution of contact variables and the development of wear scars during frictional wear processes[2]. FEM has also proven effective in simulating complex wear problems governed by frictional interactions[3]. The essential role of contact mechanics in understanding damage mechanisms and the evolution of complex stress fields has been clearly demonstrated in previous investigations[4]. Moreover, the intrinsic relationship between contact and friction has been emphasized, since frictional effects cannot occur in the absence of contact[5].

Adhesive interactions and surface roughness have also been shown to play a significant role in contact behavior. Different adhesive contact models have been analyzed to assess their applicability and limitations, with particular attention given to the unavoidable influence of surface roughness[6]. In addition, finite discrete element modeling has been introduced to determine friction forces at an equivalent single contact point, leading to a reduction in computational cost while preserving physical accuracy[7]. Classical continuum mechanics formulations have been adopted in several studies to solve contact problems[8,9], whereas discontinuum mechanics approaches have been applied to capture more complex contact behaviors and interactions[10,11].

Considerable attention has also been devoted to fretting fatigue and the influence of contact loading. Numerical investigations have demonstrated the effect of contact conditions on crack parameters in

*Corresponding author: E-mail: mahmoudi.noureddine@yahoo.fr

two-dimensional fretting fatigue problems[12,13]. Three-dimensional FEM has further been employed to characterize stress intensity factors in modes I, II, and III, as well as the J-integral, under contact fatigue conditions[14]. Additional studies have examined the influence of contact parameters on fatigue behavior, highlighting their critical role in damage initiation and propagation[15].

Experimentally, the frictional behavior between contacting surfaces has been investigated using advanced measurement techniques. High-resolution interferometric methods have been developed to measure friction forces between thin solid films[16]. In most engineering applications, friction is commonly characterized by a single coefficient, despite the inherent complexity of contact interactions[17]. Numerous numerical approaches have been proposed to simulate fracture and contact problems, including the numerical manifold method, meshless techniques[18,19], boundary dynamics[20], full discrete element methods[21], discontinuous deformation analysis[22], phase-field approaches[23], and four-dimensional lattice spring models[24].

Several investigations have addressed frictional stress distribution and dynamic effects in contact systems. It has been reported that the ratio of tangential to normal stress is not uniform and varies across the contact area in rolling mechanisms[25]. The influence of vibration on frictional response in quasi-static systems has also been examined[26]. Experimental observations have demonstrated that accurate friction prediction requires a correct evaluation of the real contact area, particularly under sliding conditions[27,28]. Additional studies have contributed to the understanding of real contact zone formation and the role of multi-asperity interactions[29-31]. It has further been shown that tangential stress within the contact region tends to remain nearly constant and independent of indentation depth and loading history[32]. Advanced methodologies aimed at reducing friction and vibration have also been developed, with applications in precision positioning systems[33].

Recent findings have shown that the friction force does not necessarily exhibit a linear dependence on the normal load[34,35]. To improve numerical accuracy, enhanced discrete element formulations incorporating boundary information have been introduced to ensure continuity of the contact normal direction[36]. Mesh-size dependency in contact force calculations has been addressed through the definition of contact potentials based on a unified characteristic length[37]. Further developments include distance-based contact potentials for arbitrarily shaped particles[38], as well as smooth contact potential algorithms ensuring continuity in both the normal direction and force magnitude[39].

In this context, the present study aims to contribute to the understanding of mixed contact behavior in elastoplastic materials through a detailed numerical investigation based on the Adaptive Mixed Contact Finite Element Method (AMC-FEM). The analyzed configuration involves contact between a rectangular plate and one or two round wires, representing a typical mixed contact situation encountered in practical engineering applications such as fretting, wire-supported structures, and tribological interfaces.

The main objective of this work is to analyze the influence of geometric parameters and frictional conditions on contact behavior. In particular, the effects of the round wire diameter and the distance between two contact points are investigated, together with the impact of different coefficients of friction. The study focuses on the evolution of key contact variables, including the real contact area (CAREA), the normal contact force (CFN), the contact position, the artificial strain energy, and the distribution of von Mises equivalent stress.

An elastoplastic material model is adopted for both contacting bodies, allowing the identification of stress concentration, local plastic deformation, and energy dissipation mechanisms within the contact zone. Both single-contact and double-contact configurations are examined to highlight interaction effects between neighboring contacts and their influence on stress redistribution and contact pressure evolution.

Finally, the numerical results obtained using the AMC-FEM approach are compared with Hertzian elastic contact theory. Good agreement is observed in the elastic regime, while additional insights are provided into non-linear effects associated with plasticity, friction, and contact geometry. The proposed numerical framework thus offers a robust tool for the analysis of mixed contact problems and contributes to the optimization of contact design parameters in elastoplastic systems.

2 Contact Modeling

2.1 Master Slave Contact

Contact between two surfaces is typically modeled through the frictional interaction that develops at their

interface. In finite element formulations, one surface is assigned as the *master* surface-generally the larger or stiffer body-while the other is designated as the *slave* surface, which is usually smaller or more compliant. The relationship between the master and slave surface nodes at the interface is illustrated in Fig. 1. To ensure accurate detection of contact constraints, the slave surface must be discretized with a finer mesh.

Figure 2 illustrates the mixed-contact configuration examined in this study. The cylindrical body acts as the master surface, while the rectangular plate represents the slave surface, meshed with refined quadrilateral elements. The contact zone forms at the interface where reaction forces, pressure distribution, and frictional behavior are computed. As shown in the figure, slight numerical penetration of the master nodes into the slave surface may still occur, despite the use of standard contact enforcement algorithms-an acceptable approximation within most finite element frameworks.

2.2 Geometric Relationships of Contacting Parts

The contact phenomenon can be investigated through three primary approaches: experimental, theoretical, and numerical. To apply contact stresses within these frameworks, three types of counter-bodies are typically employed (Fig. 3). Among these configurations, the sphere–plane contact setup is widely preferred in wear studies because it is easy to implement and allows direct comparison with the classical disc–pin apparatus. The cylinder-plane configuration is commonly used in the analysis of cracking mechanisms, as the loading can be idealized in two dimensions and efficiently modeled using finite element methods.

The plane-plane contact configuration has also gained increasing interest. By adjusting the edge curvature of the counter-body-where zero curvature corresponds to a perfectly straight edge-the resulting pressure distribution can be precisely controlled. This flexibility makes it possible to reproduce loading conditions that more closely resemble those encountered in real engineering applications.

2.3 Coefficient of Friction (μ)

The coefficient of friction quantifies the resistance to sliding that develops between two surfaces in contact. Two types of friction are typically distinguished: static friction, which opposes the initiation of motion and keeps an object at rest until the applied force exceeds its threshold, and kinetic friction, which acts once motion has already begun and resists the relative sliding of the bodies. The corresponding force components at the contact point are illustrated in Fig. 4. The relationship between the friction force F_f and the normal force F_N is expressed by Eq. (1);

$$F_f = \mu \times F_N \quad \ldots (1)$$

where F_f is the friction force (N), uμ is the coefficient of friction, and F_N the normal force. The coefficient of friction is defined as the ratio between the friction force and the normal force and is dimension less[40].

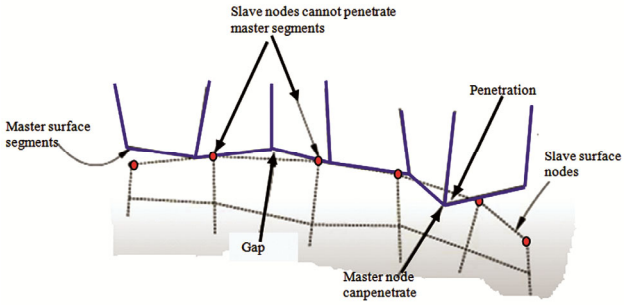


Fig. 1 — Relationship between the master and slave surfaces nodes in contact

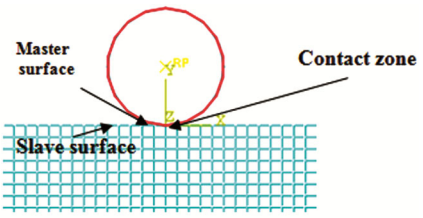


Fig. 2 — Two mixed surfaces in contact

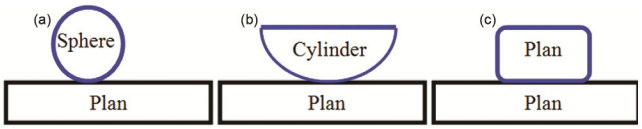


Fig. 3 — Geometric relationships used for the different contacts

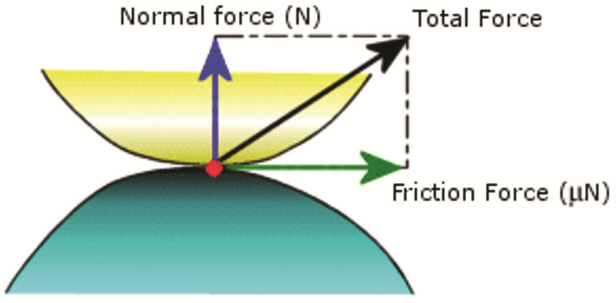


Fig. 4 — Triangle of forces at the point of contact

2.4 Illustration of Mixed Contact

As the term implies, mixed contact refers to contact that occurs between two bodies with different geometries. In the configuration considered here, one of the two bodies can be treated as having an infinite radius of curvature; in other words, the contact takes place between a cylindrical wire and a rectangular plate (Fig. 5).

To model a contact problem, a constant normal load F*N* is applied to maintain the two bodies in contact. Within the contact region, two distinct zones can be identified: an interior stick zone, of width 2c, where the surfaces remain adhered, and two slip zones located at the edges of the contact interface, where relative sliding occurs.

When the axial load P is equal to zero, the stick zone is centered within the contact region. However, when a non-zero axial load is applied, the stick zone shifts toward one side by an amount referred to as the eccentricity**.**

The normal contact pressure distribution is given by Eq. (2);

$$p(x) = p_0\sqrt{1-\frac{x^2}{a^2}} \quad \text{... (2)}$$

where p_0 is the maximum normal stress as a function of (N) and (a), the half-width of the contact area; in Fig. 5.

$$p_0 = \frac{2N}{\pi a} \quad \text{... (3)}$$

Thus, there is

$$a = \left(\frac{4NR}{\pi E}\right)^{1/2} \quad \text{... (4)}$$

The parameter (E) is the Young's modulus of the material, and (R) is the radius of the round wire. If a tangential load is applied, slippage occurs near the limits of the contact zone, while a central zone of size (2c) remains in adhesion and (μ) is the coefficient of friction.

$$\frac{c}{a} = \sqrt{1-\frac{Q}{\mu N}} \quad \text{... (5)}$$

If the force (P) is applied to the cylindrical wire simultaneously with the force (Q), an eccentricity e is

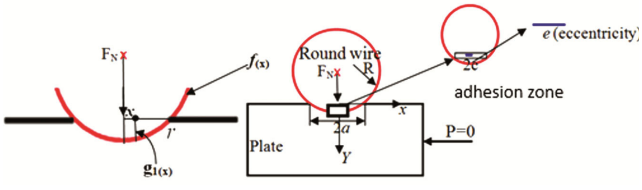


Fig. 5 — Mixed contact with applied forces

generated within the stick zone. Under these conditions, the tangential stress in the sliding zone is expressed as follows;

$$q(x) = \mu p_0\sqrt{1-\frac{x^2}{a^2}}\,|x| \le a|x-e| \ge c \quad \text{... (6)}$$

while in the adhesion zone it is equal to;

$$q(x) = \mu p_0\sqrt{1-\frac{x^2}{a^2}} - \frac{c}{a}\mu p_0\sqrt{1-\frac{(x-e)^2}{c^2}}\,|x-e| \le c \quad \text{... (7)}$$

The eccentricity of the adhesion zone is given by Eq. (8);

$$e = \frac{a\sigma}{4\mu p_0} \quad \text{... (8)}$$

where (σ) is the axial stress in the wire due to the load (P).

$$g_1(x) = R - f(x) \quad \text{... (9)}$$

The relationship of the normal force with (E) is given by Eq. (10);

$$\Delta f(x) = E g_1(x)\Delta x \quad \text{... (10)}$$

With

$$g_1(x)(\pm r) = 0 \Rightarrow R = f(r) \quad \text{... (11)}$$

The function f(x) of wire is presented by Eq. (12);

$$f(x) = |x|\int_0^{|x|}\frac{\acute{f}(x)}{\sqrt{x^2-r^2}}d(r) \quad \text{... (12)}$$

From Eq. (11), the term x can be replaced by the term r, yielding Eq. (13);

$$f(r) = \frac{2}{\pi}\int_0^r \frac{f(x)}{\sqrt{r^2-x^2}}d(x) \quad \text{... (13)}$$

The relationship between the normal force (F*N*), the force applied at the center of the round wire center part and the penetration into the second part is given by Eq. (14);

$$F_N E\int_{-r}^{r} g_1(x) = 2E\int_0^r [R - f(x)]\,d(x) \quad \text{... (14)}$$

Equation (15) presents the Young's modulus (E) for the two contact parts;

$$\frac{1}{E}\frac{1-v_1^2}{E_1} + \frac{1-v_2^2}{E_2} \quad \text{... (15)}$$

where E1 and E2 are the Young's moduli of the contacting bodies, and ν1 and ν2 are their respective Poisson's ratios[26].

2.5 Description of AMC-FEM

In the present work, the term AMC-FEM refers to an Adaptive Mixed Contact Finite Element Method specifically developed for nonlinear elastoplastic

contact simulations. and is a numerical approach to solving contact mechanics problems, which address the interaction of bodies in contact under the action of external forces. The above method encapsulates three significant aspects:

The Finite Element Method (FEM) breaks a complicated structure down into many components so as to approximately solve the governing equations.

Mixed technology solves more than a single physical variable concurrently, like finding displacement and calculating contact pressure (or stress). This results in higher contact simulation accuracy.

Adaptive mesh refinement makes it possible to improve the finite element mesh in the areas of rapid changes of the results, e.g., at the contact interface or near the crack tip, while the mesh remains rather coarse at other locations, enhancing its operational efficiency.

In this work, the Adaptive Mixed Contact Finite Element Method (AMC-FEM) is implemented using Abaqus/Standard with a surface-to-surface contact formulation. The contact constraints are enforced through the contact algorithm available in Abaqus, where the normal behavior is defined using the hard contact formulation and the tangential behavior is modeled using the penalty friction formulation. Furthermore, The AMC-FEM solution procedure involves several key steps;

i. The finite element method begins with an initial mesh being created between the bodies in contact.
ii. The adopted contact variables are initialized, and the interfaces of the bodies in contact are recognized.
iii The solution of the mixed finite element equilibrium is performed using the current contact states of the bodies.
iv. The contact gap is determined and the contact pressures are updated using the augmented Lagrange formulation.
v. The discretization error is estimated properly in a posteriori error estimator.
vi. The mesh is refined adaptively in areas with large errors (near the interface and regions with stress concentration).
vii. Repeat all the steps until the nonlinear convergence criteria and error tolerance are met.

At each iteration, the contact status (active or inactive) is updated until convergence is achieved.

Adaptive Mesh Refinement

After each converged load increment, a posteriori error estimator identifies the elements requiring refinement. Mesh refinement is concentrated near the contact interface and regions with high stress gradients while maintaining a coarser mesh elsewhere. This adaptive strategy significantly improves computational efficiency without compromising solution accuracy.

In general, the AMC-FEM combines a mixed finite element formulation, augmented Lagrange contact enforcement, Newton–Raphson nonlinear iterations, and adaptive mesh refinement to provide an accurate, stable, and computationally efficient framework for solving complex contact mechanics problems.

3 Numerical Model

3.1 Model Description

In this model, the geometric dimensions were set to a height H=50 mm and a width L=100 mm. The first part of the study was conducted to evaluate the influence of the round-wire diameter on the contact behavior between the two bodies; wire diameters of 5, 10, and 15 mm were considered. In the second part of the study, the effect of the spacing L between the two round wires was examined, with values of 20, 25, and 33 mm.

The rectangular plate was modeled using two-dimensional, 4-node quadrilateral plane-strain reduced-integration elements (CPS4R). The round wire was modeled using R2D2 elements, which are 2-node, 2D linear rigid elements suitable for plane-strain or plane-stress analyses. A total of 5232 elements and 5582 nodes were generated in the finite element mesh.

Coefficients of friction of 0.3, 0.5, and 1.0 were assigned. The assembly was defined with an elastoplastic aluminum alloy material. A normal load of F_N=3N was applied at the center of the round wire (Rp1), while a fixed constraint was applied to the bottom surface of the rectangular plate.

3.2 Mesh Convergence Study

The mesh comparison shown in Table 1 has concluded that the best option for finite element analysis is a 1.0 mm mesh size. The conclusion was reached after

Table 1 — Mesh comparison with different global element sizes

Global Size (mm)	Elements	Nodes
2.0	1308	1450
1.5	2325	2480
1.0	5232	5582
0.5	20928	21700

analyzing the accuracy and efficiency of the computations. Using 1.0 mm instead of 2.0 mm has caused a major increase in the total number of elements, from 1308 to 5232, as well as nodes, from 1450 to 5582. Moreover, the the 1.0 mm mesh allows better representation of the model geometry and accurate calculations of parameters such as stress and strain.

An additional refinement to a global size of 0.5mm results in a mesh density increase of about 20928 elements and 21700 nodes, approximately four times that achieved with a mesh of 1.0mm. Although this refinement could result in slight numerical accuracy improvement, the computational cost of obtaining it is substantial in terms of processing time, memory consumption, and solver requirements. In most cases, these additional resources bring very little in terms of simulation results improvement after achieving mesh convergence. Thus, the 1.0mm mesh is the most optimal trade-off between the accuracy of results and their computational cost. It provides a good level of refinement necessary for accurate model mechanical performance analysis while still being efficient in terms of computation time and resources required. Hence, this mesh size was used in all further finite element analysis.

Choosing the mesh of 1.0 mm also assures the accuracy and consistency of the numerical results. At this degree of refinement, the mesh is adequately dense to reduce the discretization errors without the excessive computational effort required by a very much finer mesh. Thus, the numerical simulations achieve the right combination of the required level of precision, efficiency, and practicality, which makes the mesh 1.0 mm the best choice for this study.

Mesh convergence analysis was performed by progressively refining the finite element mesh from 1308 to 20928 elements. The numerical response stabilized with increasing mesh density, indicating that the solution became practically mesh-independent. In particular, the comparison between the 1.0 mm and 0.5 mm mesh sizes showed only negligible differences, demonstrating that further mesh refinement had no significant influence on the predicted results. Therefore, the 1.0 mm mesh was selected for all subsequent simulations because it provides an appropriate balance between numerical accuracy and computational efficiency.

3.3 Material

Table 2 presents the mechanical and physical properties of the material (elastoplastic aluminum alloy). The plastic yield values are specified within the range of 80 to 120 MPa.

Table 2 — Mechanical and physical properties of the material

	Plastic		Elastic		
	Yield stress [MPa]	Plasticstrain %	Modulus of elasticity, [GPa]	Poisson's ratio	Density, kg/m^3
1	80	0	70	0.3	7872
2	120	0.3			

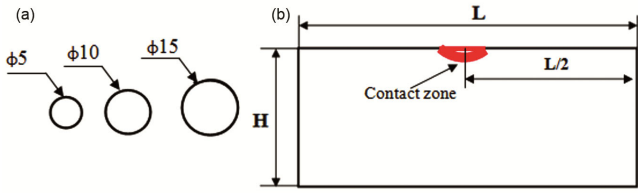


Fig. 6 — Geometric model (a) wire diameters considered (φ=5, 10, 15 mm); and (b) rectangular plate with its dimensional characteristics and the location of the contact zone

4 Results and Discussion

4.1 Single-Contact Model by AMC-FEM

In this part of the study, the contact configuration involving a round wire and a rectangular plate is presented. The model used to investigate this single-contact configuration is illustrated in Fig. 6, where three wire diameters (φ=5, 10, and 15 mm) are considered. The corresponding contact location on the rectangular plate is also shown, with the contact zone positioned at mid-length. The finite element representation of this configuration is provided in Fig. 7. An elastoplastic material model was assigned to both bodies. The rectangular plate was meshed using CPS4R elements, generated through a parametric meshing procedure, while the round wire was modeled with 2-node R2D2 rigid elements. The applied normal load F_N was introduced at the designated reference point (Rp1), directly above the contact zone.

Figures 7 (a) and (b) present the numerical model adopted for the analysis of the single-contact configuration between a cylindrical wire and a rectangular plate. Figure 7 (a) illustrates the undeformed geometry and applied boundary conditions, while Fig. 7 (b) shows the corresponding finite element discretization, with the contact interface clearly identified.

In Fig. 7 (a), the cylindrical wire is positioned above the flat surface of the plate and loaded through a reference point (RP_1), where the normal force is applied. The bottom surface of the rectangular plate is fully constrained to prevent rigid body motion and to

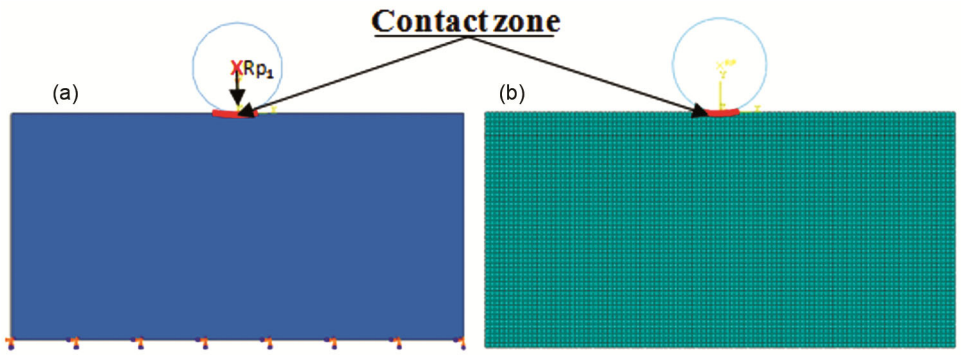


Fig. 7 — AMC-FEM model for the single-contact configuration (a) boundary conditions and loading applied at the reference point; and (b) parametric mesh generated using CPS4R elements for the rectangular plate

ensure stable transmission of contact loads. This configuration corresponds to a classical cylinder–plane contact, which is widely adopted in contact mechanics as a representative model for line-contact problems commonly encountered in fretting, wear, and load-transfer systems. Such simplified configurations enable an accurate investigation of local stress fields and contact pressure distributions while maintaining computational efficiency[41].

Figure 7 (b) presents the finite element mesh associated with the model. A locally refined mesh is introduced in the vicinity of the contact zone to accurately capture steep stress gradients, contact pressure evolution, and the development of localized plastic deformation. Outside the contact region, a coarser mesh is employed to reduce the overall computational cost. This meshing strategy is essential for ensuring numerical convergence and reliable stress evaluation in frictional and elastoplastic contact simulations[42,43]. The use of reduced-integration quadrilateral elements further enhances numerical efficiency, while requiring careful monitoring of artificial strain energy.

Figure 8 illustrates the single-contact models corresponding to different wire diameters, which constitute a key parameter in the present investigation. Variations in wire diameter directly modify the curvature of the contacting body, thereby influencing the size of the contact area, the contact pressure distribution, and the intensity of stress concentration. According to classical Hertzian elastic contact theory, an increase in wire radius leads to a wider contact region and a reduction in peak contact pressure for a given normal load. Under elastoplastic conditions, however, deviations from purely elastic behavior arise, particularly near the onset of yielding and in the presence of friction[44,35].

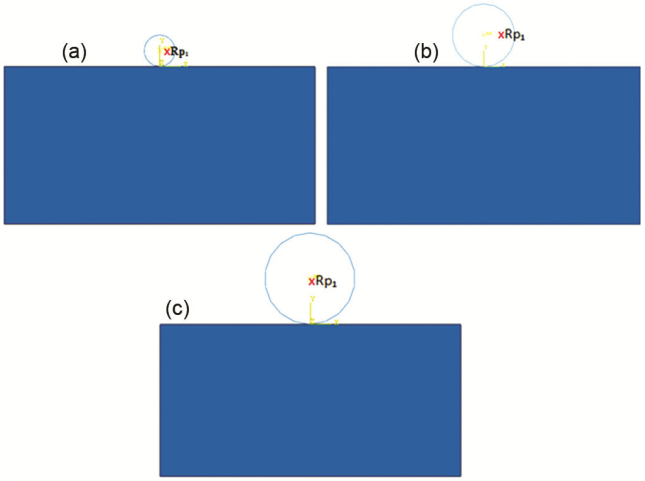


Fig. 8 — Illustration of the single contact model between the flat part and the round wire (a) the round wire: of diameter 5 mm (b) the round wire of diameter 10 mm; and (c) the round wire of diameter 15 mm

The comparison of different wire diameters shown in Fig. 8 allows a systematic assessment of geometric effects on the evolution of the real contact area, stress redistribution, and energy dissipation mechanisms. Experimental and numerical studies have confirmed that contact geometry plays a dominant role in governing wear initiation, plastic zone development, and fatigue damage in tribological contacts[45,46]. Consequently, the modeling strategy illustrated in Figs. 7 and 8 provides a physically consistent and numerically robust framework for analyzing mixed elastoplastic contact behavior.

Figure 9 illustrates the pressure distribution in the contact zone for the single-contact configuration under a friction coefficient of COF = 0.5, considering wire diameters of 5, 10, and 15 mm. For the smallest diameter (φ = 5 mm), the contact pressure is highly concentrated beneath the wire, with a pronounced maximum at the center of the contact region due to

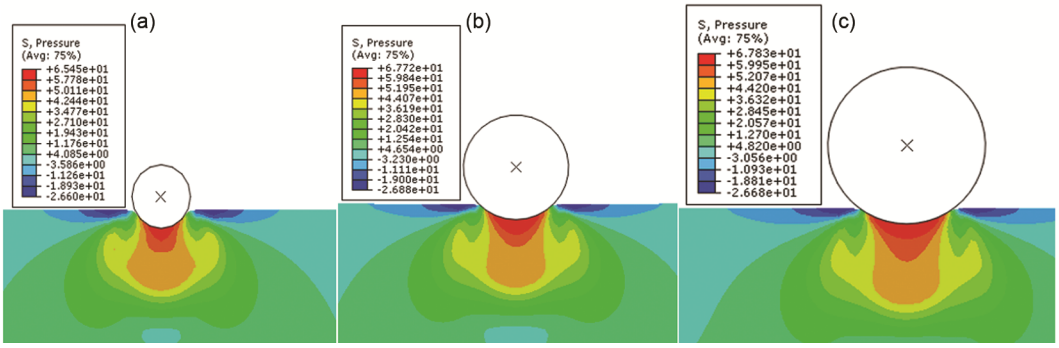


Figure 9 — Pressure state at the contact zone in the case of COF=0.5 (a) round wire with diameter 5 mm (b) round wire with diameter 10 mm; and (c) round wire with diameter 15 mm

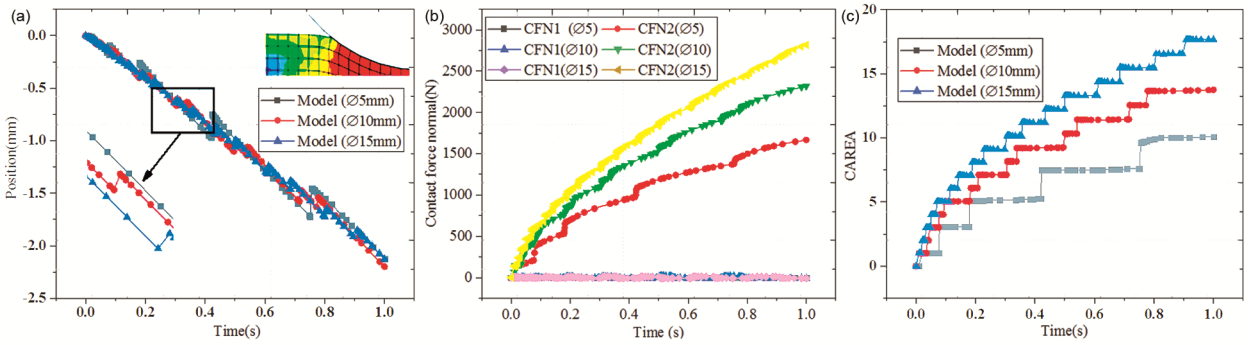


Fig. 10 — Contact state between the two parts concerning the different diameters of round wire; (a) the contact position, (b) the normal contact force along (x and y); and (c) the contact area in the case of COF = 0.5

the reduced radius of curvature and the limited contact area. Increasing the wire diameter to 10 mm leads to an expansion of the contact zone and a noticeable reduction in the peak pressure, resulting in a smoother and more homogeneous pressure distribution. For the largest diameter (φ=15 mm), the pressure field becomes significantly more uniform and the maximum contact pressure is markedly reduced, indicating a more favorable redistribution of the applied load. In all cases, the presence of friction induces a slight asymmetry in the pressure contours, reflecting the coupling between normal and tangential stresses typical of frictional contact. These observations are fully consistent with classical Hertz-Mindlin contact theory and elastoplastic contact models, which predict a decrease in maximum contact pressure with increasing radius of curvature and the redistribution of stresses under frictional loading[47-49].

4.1.1 The Effect of Wire Diameter On Contact Surface

Figure 10 presents the time evolution of the contact response for the three wire diameters (Ø 5, Ø 10, and Ø 15 mm), clearly highlighting the role of geometry in governing the contact mechanics behavior. As shown in Fig. 10 (a), the contact surface displacement becomes increasingly negative over time for all cases, indicating a progressive increase in indentation depth caused by sustained loading and local elastoplastic deformation at the contact interface. Although the overall trends are similar, small differences between the curves suggest that the wire diameter influences both the rate and magnitude of penetration, with larger diameters generally exhibiting a more gradual and stable indentation response. Figure 10b shows a continuous increase in the normal contact force (CFN) with time, with the highest force levels observed for the largest diameter (Ø15) and the lowest for the smallest (Ø5), reflecting the greater load-carrying capacity associated with larger contact radii. This trend is further supported by Figure 10c, where the actual contact area (CAREA) increases in a stepwise manner over time, a behavior typically associated with progressive surface conformity and localized plastic accommodation. The Ø15 wire exhibits the largest growth in contact area, followed by Ø10 and Ø5, indicating that larger diameters promote a more extensive real contact surface. From a physical standpoint, the increase in contact area with wire diameter leads to a redistribution of contact pressures and enhanced

normal force transmission, which has been shown to significantly influence frictional dissipation, wear mechanisms, and contact lifetime. Recent experimental and numerical studies confirm that increasing the contact size or diameter results in larger real contact areas and higher normal forces, thereby altering wear behavior and improving durability[50,51]. In addition, recent indentation and contact modeling investigations report a strong dependence of indentation depth and contact pressure on contact geometry, in good agreement with the trends observed in Fig. 10 (a)[52,53].

4.1.2 The Effect of Time Increment On Stress Variation

Figure 11 illustrates the stress variation along the true distance of the path for three increments: 10 mm, 20 mm, and 30 mm. In all cases, a pronounced central trough is observed, where stress becomes strongly negative at the center and gradually rises toward values close to zero away from the center, indicating localized stress relaxation. The trough is deeper for the 30 mm increment than for the 10 mm increment, suggesting that increasing the advancement step promotes greater relaxation and expands the affected zone, in agreement with recent studies on residual stress redistribution and crack propagation[54,55]. Although the overall shape of the curves remains similar, both the amplitude and the exact location of the minimum vary with the increment, reflecting the direct influence of this parameter on local mechanical behavior. The observed distance intervals (e.g., 15-25 mm) are also affected by contact geometry and support stiffness, which alter normal stress distribution, friction, and local mechanical energy, highlighting the need for mesh sensitivity and convergence studies[56]. The friction coefficient further affects stress and contact pressure distributions in tight fits, potentially amplifying local stress concentrations[57]. Finally, the analysis of different wire diameters (5, 10, and 15 mm) shows that increasing the diameter extends the true path length and the stress concentration zone, revealing a physical period during which stress is concentrated at the center before redistributing within the material. This observation reflects the physical mechanism of local elasto-plastic relaxation, where partial plastic deformation around the contact leads to stress redistribution and the formation of a central stress trough[54,55]. Collectively, these results confirm the effectiveness of the AMC-FEM method in capturing local stress concentration and relaxation phenomena.

4.1.3 The Effect of Friction Coefficient On Artificial Strain Energy

Figure 12 shows the artificial deformation energy as a function of time for the three cases of friction coefficient (COF): 0.3, 0.5, and 1.0. Thus, for all three diameters. It seems that for a higher COF, the

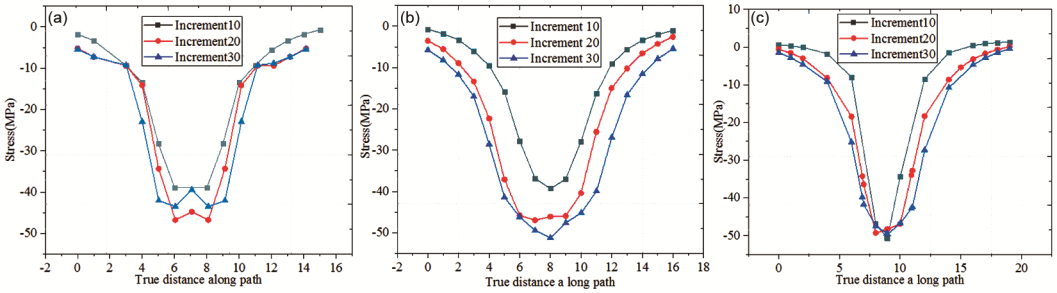


Fig. 11 — Distribution of the equivalent Von Mises stress (a) 5 mm diameter wire (b) 10 mm diameter wire; and (c) 15 mm diameter wire

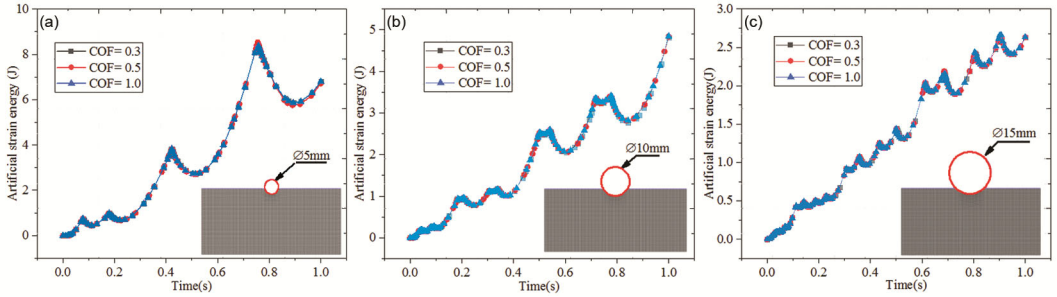


Fig. 12 — Artificial strain energy variation for the single-contact model in the case of COF = 0.3, 0.5 and 1.0: (a) 5 mm (b) 10 mm; and (c) 15 mm

artificial energy is greater and/or increases more quickly, which indicates that friction generates more dissipation or internal efforts (contact/tangential) that do not solely translate into "useful" deformation. Also, depending on the distance or position of the contact (distance mentioned as 25 mm, 20 mm, and 15 mm in the three figures), the closer to the edge or contact, the more it can influence the slope or energy peaks: the geometry of the contact, local stiffness, etc., modify how the sliding or micro contact zones activate. The higher the friction, the higher the artificial energy The results indicate that high friction causes greater dissipation and more "unnecessary" energy stored or lost[58]. It can also be observed the influence of geometry or contact position on the variation of energy/deformation and temporal variation and the presence of peaks or sudden breaks in the evolution of energy. Sources of artificial energy: In many simulations with contact, the more friction increases, the more "artificial" energy increases. Maybe what the solver introduces as a regularization or penalty term or as work from non-recoverable friction (dissipation). On the other hand, the decrease in the diameter of the round wire causes a much greater variation in artificial strain energy in the contact area. The artificial strain energy variation range is confined between 0 and 9 J for the 5 mm diameter, is confined between 0 and 5 J for the 10 mm diameter, and for 15 mm, the range is confined between 0 and 2.75 J.

4.2 Two-Contact Model by AMC-FEM

This part of the study presents a model describing the interaction of two contact regions between a cylindrical wire and a rectangular plate (Fig. 13). Both components were modeled using an elasto-plastic material behavior. The cylindrical wire has a diameter of 10 mm. Figure 14 illustrates the two-contact configurations for center-to-center distances of L = 20, 25, and 33 mm. The corresponding AMC-FEM model, including its boundary conditions and mesh of CPS4R elements, is presented in Fig. 15.

Figure 16 shows the pressure distribution at the contact between two interacting cylindrical (or spherical) surfaces and a plane.The colored areas range from blue (low pressure) to red (maximum pressure) according to the scale on the left of each Fig. 16 (a, b, and c).

- A high concentration of pressure is observed at the center of the contact.
- This indicates that the contact surface is smaller, so the maximum pressure is higher.
- This indicates that the contact surface is smaller, so the maximum pressure is higher. The material locally undergoes more intense stress, risking the onset of plasticization or increased wear.

In the case of L = 25 mm, the red zone slightly expands, and the yellow-green contours become more extensive. This shows a better distribution of pressure. On the other hand, increasing L (the distance between centers) leads to a reduction in the maximum pressure, even though the total contact area increases. If L = 33 mm, the central red zone decreases even further: the pressure becomes more uniform. This indicates that the system is moving toward a softer and better-distributed contact. On the other hand, localized stresses decrease, so the risk of deformation or damage is reduced. These results are explained by Hertz's theory on elastic contact;

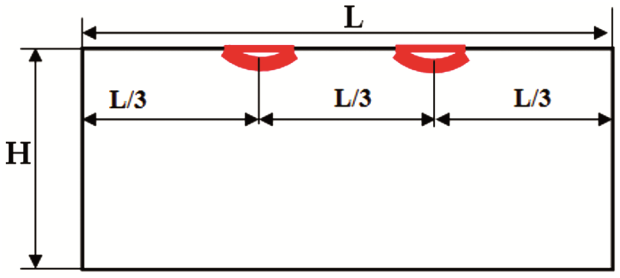


Fig. 13 — Geometric model two-contact with the presentation of dimensions

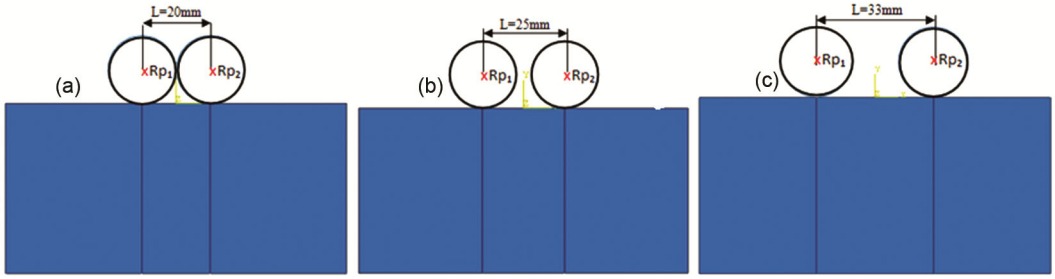


Fig. 14 — Illustration of the two-contact model based on the distance between them (a) L = 20 mm, (b) L = 25 mm; and (c) L=33 mm

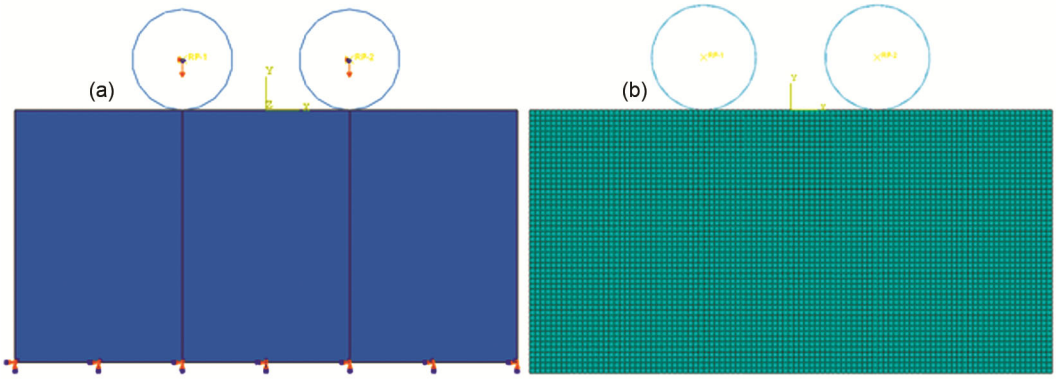


Fig. 15 — AMC-FEM model with two contacts (a) boundary conditions; and (b) model mesh

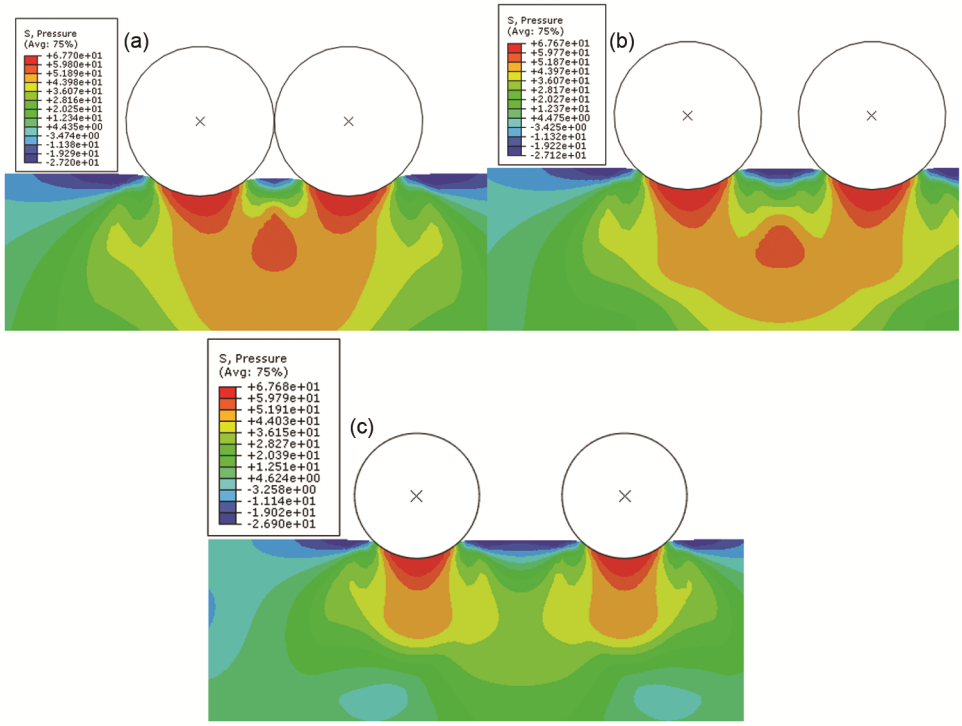


Fig. 16 — The pressure state at the contact zones in the case of COF=0.5 (a) L= 20 mm, (b) L=25 mm; and (c) L=33 mm

- When the contact surface increases (increase in L or the contact geometry), the maximum pressure decreases.
- Conversely, a smaller contact surface leads to higher contact pressure.

4.2.1 The Effect of the Distance Between the Two Cylinders on the Contact Surface

A clear decreasing relationship (position as a function of time) with a regression line and some small deviations. This looks like an elastic contact law or a log-log representation where the slope translates to an exponent (e.g., Hertzian behavior or an elasticity/plasticity model). Interpretation: The mechanical response follows a regular law dominated by geometry/rigidity (Hertzian or modified contact law), with some local transitions (hysteresis or micro-adhesions). Implication of importance: Slope and deviation from the straight lines provide information about the elastic vs adhesive/viscoelastic nature of the contact. On the other hand, Fig. 17 (b) is a curve that shows an accumulation and other curves that remain low (a circled area). This looks like a graph of the type "cumulative contact area vs displacement/force" or "number of contact points/contact area vs time/depth": the staircase indicates the successive appearance of new contact points/patches (discontinuous contacts). The evolution for both parameters increases and for the contact position

decreases. The results indicate that the normal contact force CFN2 increases while CFN1, remains zero over the time, this is because the contact reaction develops mainly along the Y-axis, which represents the perpendicular direction to the contact surface. In this case, the perpendicular component of the contact force increases in the Y-axis direction represented by (CFN2), while the perpendicular component of the force remains almost zero in the X-axis direction represented by (CFN1) because there is no contact reaction present in this direction. In other words, CAREA values increase with increasing time. It is noted that the slightly higher value is recorded for L=33mm. However, the state of contact area has been shown in Fig. 17 (c), it can be noticed that this state is proportional in the time interval for the different distances studied.

Furthermore, Fig. 17 (c) shows a series of regular steps (jumps), typical of an effective contact area measurement that increases in jumps, for example, when successive asperities come into contact or when adhesive junctions undergo local ruptures. The overall contact is established through discontinuous contributions from asperities/junctions; this behavior has consequences on the evolution of force and energy dissipation (hysteresis). On the other hand, there are several recent references in this field, such as the work proposed[44], a review on adhesion models and heterogeneous contacts useful for understanding multiple contact areas (shows transitions where the contact area decreases despite the increase in payload if it is observed that folds/drops)[59,28] experimental/FEM procedure and effective area corrections are useful for interpreting indentation and contact area measurements.

4.2.2 The Effect of Time Increment on Stress Variation

Figure 18 shows the variation of stress as a function of true distance a long path. In the three sub-figures, two localized stress peaks (on the order of ~90-110 MPa according to the figure) separated by a central zone where the stress drops sharply (~0-20 MPa). The three series "increment 10, 20, and 30" generally follow the same shape but with small differences. On the other hand, the effect of the increment size is that the series with the largest increment (30" increment) generally tends to give slightly higher maximum values and more pronounced oscillations/locals at the peaks compared to the finer increments (10 or 20). In other words,

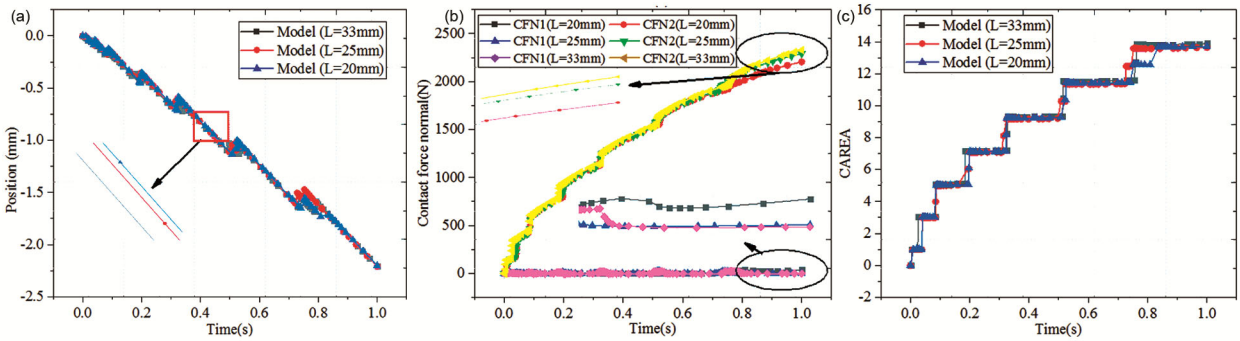


Fig. 17 — Contact state between the two parts concerning the second double contact model in the case of COF=0.5, (a) the contact position (b) the normal contact force along (x and y); and c) the contact area

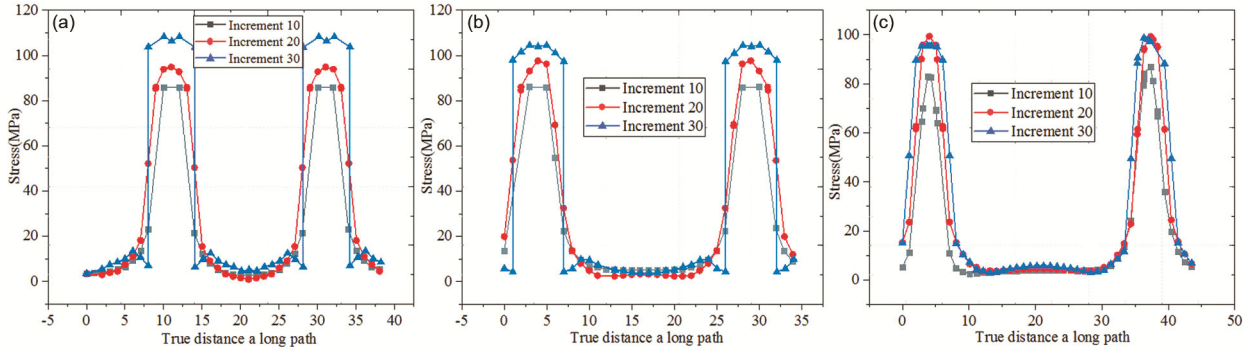


Fig. 18 — Distribution of the equivalent Von Mises by the stress by the AMC-FEM method concerning the two contacts, (a) L=20 mm, (b) L=25mm and (c) L=33 mm

increasing the increment size can overestimate peak values and make the curve less smooth. This is typical when the temporal resolution/loading is not fine enough to properly follow the local non-linearity. It is also observed that the stress value for both cases, L=20mm and L=25mm, is slightly higher compared to the case of L=33mm. However, it can also be observed that the distance between the two contacts is well respected. That is, the stress distribution is quite fair, and the stress range is confined between 0 and 110 MPa by the AMC-FEM method. Moreover, the difference between increment 10 and increment 20 is smaller than that between 10 and 30, which suggests that the solution converges as the increment decreases; it is necessary to verify that the difference becomes negligible to decide on an acceptable increment for the convergence criterion in this comparison. Good practice for convergence testing and error estimation under these conditions has been reported in the literature[60]. For convergence and refinement[42] to understand the effect of the mesh on stress peaks. Heterogeneous adhesion and contact models are useful for understanding interactions between multiple contact zones[61]. The three graphs show the same physical phenomenon but with different numerical sensitivity. In physics, the area's most sensitive to geometry and material models are corners, edges, contacts, and singularities. On the other hand, in numerical methods, there are two main causes: increment size (no loading / no time) and mesh / elementary integration.

4.2.3 The Effect of Friction Coefficient on Artificial Strain Energy

Figure 19 illustrates the evolution of artificial strain energy over time for three coefficients of friction (COF ≈ 0.3, 0.5, and 1.0). In all cases, a general upward trend is observed, accompanied by periodic oscillations or repeated peaks, whose amplitudes notably increase toward the end of the simulation. For most of the simulation time, the three curves largely overlap, but toward the end, the case with COF = 1.0 exhibits slightly higher values and more pronounced fluctuations compared to COF = 0.3 and 0.5, indicating that higher friction slightly increases artificial energy and temporal variability, particularly during periods of significant sliding.

The signals also display localized jumps, which likely correspond to contact transitions, such as stick-to-slip events, engagement of new contacts, or large relative displacements. Physically, these peaks reflect rapid changes in the local stress state, where small regions of the mesh undergo elastic–plastic adjustments captured numerically as artificial energy. Artificial strain energy is primarily a numerical quantity, arising from solver mechanisms such as hourglass control, reduced integration schemes, or penalty-based contact enforcement. Excessive values or rapid increases indicate numerical artifacts, including instabilities, hour glassing, or poorly resolved contact, which can distort the physical interpretation of results.

Analysis of distance effects reveals that for the smallest contact distance (L = 20 mm), disturbances appear in the time interval 0.6–1.0 s, whereas for larger distances (L = 25 mm and 33 mm), artificial energy remains well-proportioned and consistent across COF values. This behavior can be physically interpreted as contact proximity amplifying local stress gradients, which intensifies local plastic deformation and micro-sliding, leading to increased artificial energy. Interestingly, for L = 20 mm, the highest artificial energy occurs for COF = 0.3, likely because the smaller separation gap concentrates contact forces, making even moderate friction produce significant local energy accumulation.

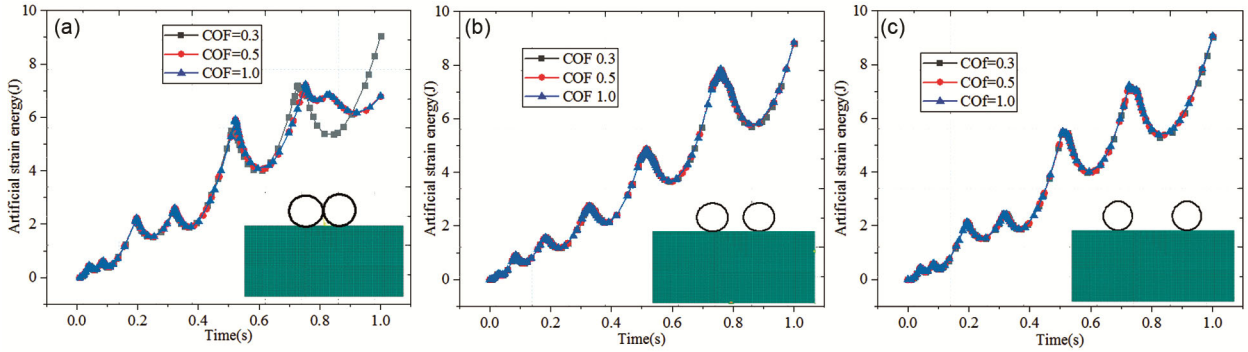


Fig. 19 — Distribution of artificial strain energy by the AMC-FEM method concerning the two contacts, (a) L=20 mm (b) L=25mm; and (c) L=33 mm

Wire diameter also affects artificial energy: smaller diameters exhibit larger variations because the contact area represents a larger proportion of the total volume, so local frictional effects are more pronounced. Larger diameters distribute stress and deformation over a greater volume, reducing artificial energy magnitude. These observations are consistent with studies showing that friction, contact geometry, and solver formulations (penalty, Lagrange multipliers, surface-to-surface contact, hourglass control, and reduced integration) strongly influence artificial energy and numerical stability[62,7,63].

It has been demonstrated that an increase in the coefficient of friction (COF) intensifies the development of plastic zones and significantly alters stress distributions, in agreement with the trends observed in the present results[57]. Higher COF values lead to larger localized plastic deformations and steeper stress gradients, which in turn result in increased artificial strain energy. Certain finite element formulations, such as reduced-integration brick elements (e.g., C3D8R), may accumulate a substantial portion of artificial energy when mesh density or solver parameters are not appropriately selected. To address these numerical artifacts, recent methodologies have been proposed, including assumed enhanced strain (AES) formulations, stress smoothing techniques, and advanced surface-to-surface contact algorithms for large displacements. These approaches aim to reduce contact pressure oscillations and improve energy distribution, thereby enhancing the accuracy and reliability of frictional contact simulations.

In summary, the observed trends of increasing artificial energy with higher COF and smaller distances can be physically explained by enhanced local plasticity, micro-sliding at contact interfaces, and concentrated stress gradients, which are numerically captured as artificial strain energy. These findings emphasize the importance of carefully selecting mesh resolution, contact formulation, and friction parameters to minimize non-physical contributions while accurately representing the mechanics of contact and friction.

4.3 Quantitative Validation with Hertz's Theory and the FEM Method

The contact parameters derived from the Hertz theory and the finite element model are demonstrated in Table 3. According to Hertz, the actual contact width is 0.0576 mm, and the contact width obtained from FEM is 0.0545 mm, with a deviation percentage of 5.38 %. The pressure computed by Hertz is 73.7 MPa, while the FEM result indicates a pressure of 67.8 MPa, thus creating a difference of 8 %. The difference in the contact area also marks a value of 7.33 %. Such a negligible difference between the Hertz theory and finite element analysis indicates satisfactory agreement between the two approaches and thus confirms the correctness of the FEM model. The discrepancy occurs because the Hertz theory assumes simplifications regarding all the forces acting on the body and the principle of deformation of the semi-infinite plane body by the elastoplastic material.

Table 3 — Comparison of the different results between Hertz's theory and the FEM method

Parameter	Hertz Theory	FEM	Error (%)
Contact width	0.0576mm	0.0545mm	5.38 %
Maximum contact pressure	73.7MPa	67.8MPa	8%
Contact area	0.0518mm^2	0.0480mm^2	7.33 %

The calculated error rate ranged from 5.38 % to 8 %. Therefore, the results obtained are in satisfactory agreement.

5 Conclusion

This study presented a numerical investigation of mixed elastoplastic contact between a cylindrical wire and a flat plate using the Adaptive Mixed Contact Finite Element Method (AMC-FEM). The proposed numerical framework was used to examine the combined effects of contact geometry, friction, and elastoplastic material behavior under nonlinear contact conditions.

The results showed that contact geometry has a significant influence on the mechanical response of the system. Increasing the wire diameter enlarged the contact area, reduced the maximum contact pressure, and alleviated local stress concentrations. The coefficient of friction also played an important role by increasing stress asymmetry, promoting stick-slip behavior, and increasing the artificial strain energy associated with nonlinear contact interactions. The investigation of double-contact configurations demonstrated that increasing the spacing between adjacent contact regions progressively reduced the interaction between the two contact zones, leading to lower peak stresses and a more uniform stress distribution. These findings provide useful insight into the influence of contact spacing on the mechanical behavior of engineering components subjected to frictional loading. The numerical predictions showed

good agreement with Hertzian contact theory in the elastic regime while extending the analysis to elastoplastic deformation and frictional effects that cannot be described by classical analytical solutions. This agreement supports the reliability of the proposed numerical approach for nonlinear contact analysis. Overall, the proposed AMC-FEM framework provides an accurate and efficient numerical approach for analyzing mixed elastoplastic contact problems. By accounting for the combined influence of contact geometry, friction, and material nonlinearity, the developed model offers a practical basis for the analysis and design of engineering components operating under complex contact conditions.

References

1 Barber J R & Ciavarella M, Contact mechanics, *Int J Solids Struct*, 37 (2000) 29.
2 Yue T & Wahab M A, *Tribol Int*, 107 (2017) 274.
3 Mäntylä A, Juoksukangas J, Hintikka J, Frondelius T & Lehtovaara A, *FEM-based wear simulation for fretting contacts*, 53 (2020) 20.
4 Li B, Li P, Zhou R, Feng X-Q & Zhou K, *Tribol Int*, 171 (2022) 107534.
5 Zhang S, Li D & Liu Y, *Micromach*, 13 (2022) 1907.
6 Ciavarella M & Joe J A, *J Royal Soc Interface*, 16 (2019) 20180738.
7 Liu H *et al*., *Mathemat*, 11 (2023) 4197.
8 Chen H, Zhu H & Zhang L, *Rock Mech Rock Eng*, 56 (2023) 4271.
9 Moës N & Belytschko T, *Eng Fract Mech*, 69 (2002) 813.
10 Cundall P A, *Int J Rock Mechan Min Sci*, (1971) 107.
11 Huang L, Liu J, Zhang F, Dontsov E & Damjanac B, *Int J Solids Struct*, 176 (2019) 207.
12 Bentahar M, Benzaama H & Noureddine M, *Fract Struct Integr*, 15 (2021) 182.
13 Bentahar M, Noureddine M & Youcef M A, *Military Tech Courier*, 73 (2025) 136.
14 Benzaama H, Aour B, Benzaama A & Elachachi S, *Int J Numer Method Eng*, 1 (2008) 289.
15 Hamadouche F, Benzaama H, Mokhtari M & Tahar M A, *Fract Struct Integr*, 15 (2021) 228.
16 Jung J & Chen T, Experimental measurement of friction forces using interferometry, *EPJ Web of Conferences*, 2016, pp. 06002.
17 Kalin M & Jan P, *Friction*, 13 (2025) 9440986.
18 Guilkey J, *et al*., *Comput Method Appl Mech Eng*, 415 (2023) 116260.
19 Mazhar F, *et al*., *Eng Anal Bound Elem*, 124 (2021) 14.
20 Yao W W & Zhou X-P, *Eng Anal Bound Elem*, 144 (2022) 569.
21 Shao, Z *et al*., *Rock Mech Rock Eng*, 55 (2022) 4477.
22 Xu D, *et al*., *Int J Rock Mech Min Sci*, 127 (2020) 104206.
23 Yang L, *et al*., *Comp Method Appl Mech Eng*, 387 (2021) 114127.
24 Zhao G-F, *et al*., *Int J Rock Mech Min Sci*, 133 (2020) 104361.
25 Khurramov S, *et al*., Stress analysis in rolling contacts, *E3S Web of Conferences*, 2019, pp. 06017.
26 Popov M, *Front Mech En*, 6 (2020) 69.
27 Jan P, *et al*., *Tribol Int*, 191 (2024) 109171.
28 Sahli R, *et al*., *Proceed Natl Acad Sc*, 115 (2018) 471.
29 Xu Y, *et al*., *Tribol Lett*, 66 (2018) 32.
30 Zugelj B B & Kalin M, *Tribol Int*, 119 (2018) 667.
31 Zugelj B B & Kalin M, *Tribol Int*, 141 (2020) 105955.
32 Lyashenko I A, Filippov A E & Popov V L, *Mach*, 11 (2023) 583.
33 Popov V L, Advanced approaches in contact mechanics, *AIP Conference Proceedings*, 2021, pp. 020056.
34 Mishra T, *et al*., *Wear*, 436 (2019) 203042.
35 Müser M H & Nicola L, *MRS Bullet*, 47 (2023) 1221.
36 Munjiza A A, Knight E E & Rougier E, *Comp Mech Discont*, John Wiley & Sons, (2011) pp. 304.
37 Yan C & Zheng H, *Int J Nume AnalMethod Geomech*, 41 (2017) 265.
38 Zhao L, *et al*., *Int J Numer Method Eng*, 115 (2018) 238.
39 Lei Z, *et al*., *Comp Particle Mech*, 7 (2020) 807.
40 Bird J O & Chivers P, *Newnes Engineering and Physical Science Pocket Book*, Newnes, (2014) pp. 656.
41 Popov V L, Heß M & Willert E, *Handbook of Contact Mechanics*, Springer Nature, 2019.
42 Cadet G & Paredes M, *Mech Ind*, 25 (2024) 22.
43 Liu B, *et al*., *Int J Rock Mech Min Sci*, 183 (2024) 105919.
44 Argatov I, *Int J Eng Sci*, 190 (2023) 103883.
45 Simarro M, *et al*., *Tribol Int*, 196 (2024) 109708.
46 Yang D, Wang X & Hou Y, *Friction*, 14, 2025.
47 Bhushan B & Ko P L, *Appl Mech Rev*, 56 (2003) B6.
48 Hertz H, *J Pure Appl Math*, 92 (1881) 156.
49 Liu H, Zhang H & Ding X, *Adv Contact Mech*, 12 (2024) 179.
50 Persson B N J, *J Chem Phys*, 115 (2001) 3840.
51 Sanyal A, *J Tribol*, 148 (2026) 014501.
52 Feng Q, *et al*., *J Tribol*, (2026) 1.
53 Kong Y, *et al*., *Adv Function Mater*, (2026) e25682.
54 Alshoaibi A M & Fageehi Y A, *Appl Sci*, 14 (2024) 1848.
55 Baldassarre A, Effect of residual stresses on fatigue crack growth, Clarkson University, 2021.
56 Bracamonte A J, *et al*., *Appl Sci*, 13 (2023) 2352.
57 Izard E, *et al*., *Lubricants*, 13 (2025) 231.
58 Izard E, *et al*., *Lubricants*, 11 (2023) 472.
59 Li C-Y, *et al*., *Appl Mech Rev*, 78 (2026) 010801.
60 Sinclair G, Beisheim J & Roache P, *J Verif, Valid Uncert Quantif*, 1 (2016) 041003.
61 Depalle B, *et al*., *J Mech Behav Biomed Mater*, 18 (2013) 200.
62 Jahanbani A, Pirmohammad S & Ayatollahi M, *Case Stud Construct Mater*, 21 (2024) e03775.
63 Zimmerman B K & Ateshian G A, *J Biomech Engi*, 140 (2018) 081013.